RESEARCH ARTICLE

A Multifunctional 3D Bioprinting System for Construction of Complex Tissue Structure Scaffolds: Design and Application

Yuanyuan Xu[1,2,3], Chengjin Wang[1,2,3], Yang Yang[1,2,3], Hui Liu[4], Zhuo Xiong[1,2,3], Ting Zhang[1,2,3]*, Wei Sun[1,2,3,5]*

[1]Biomanufacturing Center, Department of Mechanical Engineering, Tsinghua University, Beijing 100084, China
[2]Biomanufacturing and Rapid Forming Technology Key Laboratory of Beijing, Beijing 100084, China
[3]Biomanufacturing and Engineering Living Systems" Innovation International Talents Base (111 Base), Beijing 100084, China
[4]SunP Boyuan (Beijing) Biotech Co., Ltd., Beijing 100085, China
[5]Department of Mechanical Engineering, Drexel University, Philadelphia, PA 19104, USA

Abstract: Three-dimensional (3D) bioprinting offers a potentially powerful new approach to reverse engineering human pathophysiology to address the problem of developing more biomimetic experimental systems. Human tissues and organs are multiscale and multi-material structures. The greatest challenge for organ printing is the complexity of the structural elements, from the shape of the macroscopic structure to the details of the nanostructure. A highly bionic tissue-organ model requires the use of multiple printing processes. Some printers with multiple nozzles and multiple processes are currently reported. However, the bulk volume, which is inconvenient to move, and the high cost of these printing systems limits the expansion of their applications. Scientists urgently need a multifunctional miniaturized 3D bioprinter. In this study, a portable multifunctional 3D bioprinting system was built based on a modular design and a custom written operating application. Using this platform, constructs with detailed surface structures, hollow structures, and multiscale complex tissue analogs were successfully printed using commercial polymers and a series of hydrogel-based inks. With further development, this portable, modular, low-cost, and easy-to-use Bluetooth-enabled 3D printer promises exciting opportunities for resource-constrained application scenarios, not only in biomedical engineering but also in the education field, and may be used in space experiments.

Keywords: 3D printing; Modular design; Microextrusion; Multifunctional printing

***Correspondence to:** Ting Zhang, Biomanufacturing Center, Department of Mechanical Engineering, Tsinghua University, Beijing 100084, China; t-zhang@tsinghua.edu.cn; Wei Sun, Biomanufacturing Center, Department of Mechanical Engineering, Tsinghua University, Beijing 100084, China; weisun@mail.tsinghua.edu.cn

Received: May 20, 2022; **Accepted:** June 17, 2022; **Published Online:** September 19, 2022

Citation: Xu Y, Wang C, Yang Y, *et al*., 2022. A Multifunctional 3D Bioprinting System for Construction of Complex Tissue Structure Scaffolds: Design and Application. *Int J Bioprint,* 8(4): 617. http://doi.org/10.18063/ijb.v8i4.617

1. Introduction

The field of tissue engineering is maturing for creating opportunities that provide complex tissues and organs to impact human health. A greater understanding of human pathophysiology requires the development of more biomimetic experimental systems that allow for the analysis of cell-to-cell communication and tissue-tissue interactions in more relevant organ context roles[1]. Promotion in the field of organ transplantation requires the regenerative medicine scientists to scale up and automates the process of organ construction while providing precision and reproducibility[2-4]. Three-dimensional (3D) bioprinting offers a potentially powerful new approach to reverse engineering human pathophysiology to address these long-standing problems[5-7].

The great challenge in the regeneration of functional living tissues and organs is the complexity of structural elements, ranging from the shape of the macroscopic structure to the details of the nanostructure. At the

nano- (1 nm to 1 μm) and micro-structural (1 μm to 1 mm) scale, cells proliferate, differentiate, and utilize their inherent mechanisms to form nanostructures as organ scaffolds. With the angiogenesis develops, a network of capillaries forms, providing cells with essential nutrients and growth factors. At the meso- (1 mm to 1 cm) and macrostructural (>1 cm) scale, identifiable tissues and organs are formed from various types of cells, blood vessels, extracellular matrix, etc. In general, there are four scales (levels) of complexity in the macrostructure of tissues and organs (**Figure 1A**). Flat tissues (relatively thin structure, such as the cornea, skin, and bladder) are composed of cell sheets stacked in multiple layers, and allowing for nutrient diffusion without complete vascularization; Tubular structures (such as the artery, trachea, and urethra) are composed of cell sheets formed into circular, bilayer tissues. The relatively thin wall thickness of tubular tissue enables nutrient diffusion and oxygen exchange. Large-diameter vessels are relatively easy to fabricate, while microstructural arterioles, venules, and capillaries remain a challenge; Viscus organs with hollow tubules (such as the heart, intestine, and stomach) consist of an inner layer of epithelial cells surrounded by smooth muscle and an outer layer formed with or without connective tissue. It has been demonstrated that macroscopic and partially mesoscopic structural elements of organs with hollow tubes can be fabricated *in vitro*[8]. However, reconstructing organ microarchitecture, including glands and blood vessels, remains a challenge; most complex solid organs (such as the liver, brain, and kidney) require mature vascular networks with extensive branching for cells to remain viable and function, as well as precise distribution structures of multiple types of cells[9]. Solid organs require several essential structures to restore function, whereas tubular structures are more easily recreated from basic cells and materials. Complexity can be also found at the interfaces between tissues, such as the transition from cartilage to bone in the osteochondral interface in articulating joints[10]. An increase in the level of complexity of the tissue or organ to be repaired usually requires a corresponding increase in the complexity of the tissue engineering approach. 3D bioprinting offers the best potential in deposition of biomaterials (with or without proteins, growth factor, etc.,) and cells into precise geometries to create anatomically correct living structures with multiscale.

Cellular responses to the surrounding environment are thought to play an important role in the pathogenesis from developmental morphogenesis to disease states. Cellular matrix elasticity can be used to facilitate expected cellular behavior[11,12]. Human cells and tissues have their own rigidity, ranging from a few kPa to tens of GPa (kidney[13,14], heart[15,16], skin[17,18], arterial wall[19,20], liver[21,22], prostate[23], saphenous vein[19], cornea[24,25], breast[26,27], tendon/ligament[28,29], cancellous bone[19,30], brain[31-33], cartilage[34,35], and cortical bone[36]), depending on the specific cell type, extracellular matrix, and structural organization. Biomaterials that closely mimic organ nanostructures could be used to replicate nano-to-macro approach to human organ development, and proper biomaterial placement is necessary to direct cellular self-assembly[37,38]. The elastic modulus and molding process characteristics of common printable biomaterials (collagen[39,40], fibrin[41,42], alginate[43], chitosan[44,45], agarose[46], Poly(3-Hydroxybutyrate-co-3-Hydroxyvalerate) (PHBV)[47], and other polymers[48,49]) are summarized in **Figure 1B**. To print physically similar microenvironments *in vitro*, appropriate mechanical properties and modeling processes of the materials used must be considered[50,51]. A highly biomimetic tissue/organ

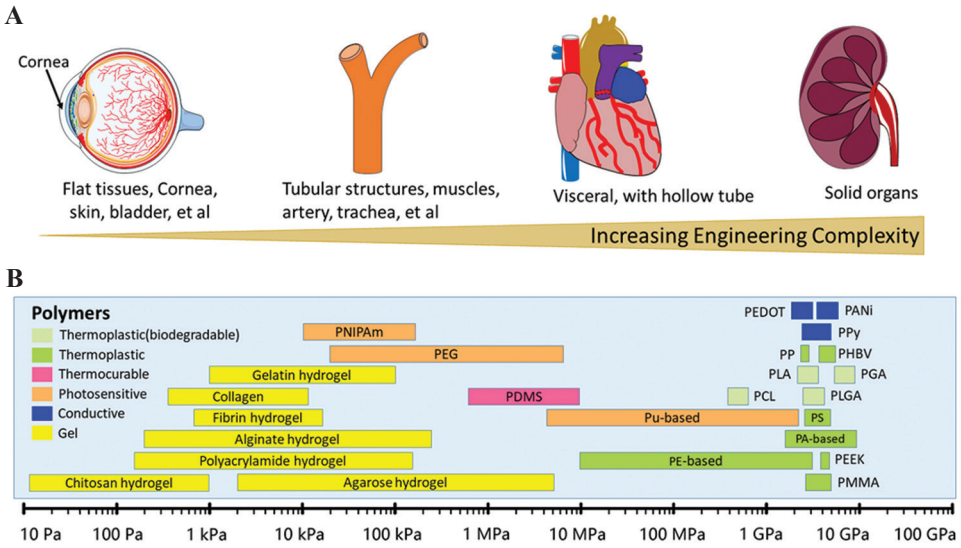

Figure 1. (A) Organ anatomy by structural complexity. (B) Mechanical properties and molding process characteristics of biomaterials.

model should be constructed by printing a variety of cells and biological materials, which requires the ability to simultaneously realize the integrated manufacturing of multiple materials and multiple printing processes in a small space. The current bioprinting capabilities rely on the mechanical placement of cells that can produce low-resolution structures (>1 cm) to very high resolutions of 20 μm. However, even the highest resolution printing methods are limited in their ability to reproduce microstructural anatomy with high fidelity. To fully realize the potential of whole-organ bioprinting, macro-to-micro (bioprinting) and nano-to-meso (biomaterial/cell self-assembly) approaches must work in harmony.

The extrusion-based 3D bioprinting strategies were among the earliest developed modalities and are now demonstrably the most widely used for fabricating 3D tissue structures[52-54]. To fabricate the previously described complex, multiscale and multi-material biomimetic tissues and organs in tissue engineering and regenerative medicine, it is necessary to provide a multifunctional 3D bioprinting system for construction of complex tissue structure scaffolds. There have been some research reports on integrated 3D bioprinting applications, for example, polycaprolactone (PCL) and meniscal fibrocartilage chondrocyte-laden GelMA/MECM bioinks which were integrated to complete the biomimetic meniscal scaffold, which had the best biomimetic features in terms of morphology and components. This approach obviously improves both the level and efficiency of biomimetic meniscal scaffolds in tissue engineering[55]. Kolesky *et al*. printed vascularized, heterogeneous cell-laden tissue constructs using multi-material of cells, and ECM. This highly scalable platform allows one to produce engineered tissue structures, in which vasculature and multiple cell types are programmably placed in the extracellular matrix[56]; Ouyang *et al*. presented a versatile bioprinting methodology using a single bioprinting step by combining two nozzles to fabricate a 3D complex blood vessel network without the need for material casting or cell post-seeding. This dual materials printing approach can also be extended beyond tissue fabrication and toward customized hydrogel-based microfluidics and self-supported perfusable hydrogel constructs[57]; Wang *et al*. presented a novel integrated printing system and fabricated a beneficial multiscale hierarchical scaffold which combined with meso-, micro-, and nano-fiber filaments. The obtained *in vitro* biological results validate the ability of multiscale hierarchical scaffolds to enhance cell adhesion and proliferation and promote cell alignment with the guidance of the aligned microfibers produced through melt electrospining writing in hierarchical scaffolds[58].

However, due to the limitations of printing processes and materials in the above reports, the scaffolds composed of hydrogel materials have low mechanical strength and are not suitable for animal experiments or long-term culture *in vitro*; Scaffolds composed of fibrous materials have poor degradation performance and cannot achieve gradient degradation. Composite scaffolds of mixed ploymer and hydrogel have no pre-vascularized channels, making it impossible to fabricate bulk tissue or organs. At the same time, it should be noted that insufficient developing work has been carried out on the miniaturization and easy-to-use of 3D bioprinting systems for wide adaptability with increasing demand on collaborative printing. The limitations of the current 3D bioprinting systems are their few printing modes, complex modeling and printing procedures, large volume and footprints, and single enabling technology results in less printable materials. The above disadvantages cause inconvenience in the operation processes and severely hinder the availability of this technology in resource-limited or special care setting points. Therefore, there is an urgent need to develop a portable, multifunctional 3D bioprinting system for construction of complex tissue structure scaffolds for laboratory, hospital, and industrial applications, which can print almost all exist biomaterials in one platform.

To achieve this goal, we present a versatile bioprinting system manufacturing methodology. A microextrusion-based modular 3D bioprinting platform was developed with total dimensions of 300 mm × 300 mm ×300 mm in width, length, and height (including the motion system, nozzle, additive manufacturing platform, cartridges, temperature controller, and UV controller system). Mechanical piston-, pneumatic-, and screw-based microextrusion processes can be implemented on this bioprinting platform. Different from the traditional design, the nozzle and the motion platform are physically separated. Each nozzle can be individually controlled, including the extrusion speed, cartridge temperature, height in the Z direction, UV light intensity, and duration. The appropriate nozzle can be selected according to one's needs, the movement platform can be connected through the designed quick-release joint, and the signal transmission can be realized. Up to three nozzles can be mounted at the same time as one needed. Modular assembly makes the replacement of nozzles more convenient. Another crucial feature of the developed bioprinting system is the Bluetooth communication possibilities, providing an accessible user interface when using PAD for remote control. This is particularly beneficial for operating the 3D bioprinter in the biological safety cabinet. Furthermore, 3D models generated from commercial 3D scanning software are facilitated by the established printing system, promoting on-demand applications. The 3D bioprinting system can print soft and hard materials, multiscale fiber filaments

(such as thick fiber filaments, thin fiber filaments, and nanofibers), and multiscale structures (macrostructure, mesostructure, and microstructure). Particular emphasis was placed on the development of resolution comparable to commercial 3D bioprinters, despite the small size and significantly lower costs. This was followed by verification of the printing competency with commercial polymer, silicone, and hydrogel (bio)inks. Meanwhile, we explored the integrated manufacturing of multiple materials and multiple printing processes. Finally, we explored the feasibility of the developed multifunctional modular 3D bioprinting system in the fabrication of tissue engineering and regenerative medicine implants, as well as bioprinting afloat. In addition, of critical importance, this portable, modular, low-cost, and easy-to-use Bluetooth-enabled 3D printer promises exciting opportunities for resource-constrained application scenarios, not only in biomedical engineering but also in the education field, and may be used in space experiments.

2. System configuration for multifunctional modular 3D bioprinting system

2.1. System configuration

The multifunctional modular 3D printing system designed in this research mainly includes the 3D motion system, material delivery system, forming environment, monitor and feedback system, electronic control system, and software operating system. Before printing, the system reads the premodeled, analyzed, and sliced files from the input device, outputs the control instructions from the software to the control board, drives the motor through the drive circuit to drive the nozzle to move in the X, Y, and Z directions, and controls the extrusion system of the nozzle to adjust the extrusion volume of the nozzle. According to the read file information, print layer by layer until the printing is completed.

Based on the need for 3D printing multiscale and multi-material structures, the system we developed can print soft materials, hard materials, and multiscale fiber filaments (**Figure 2**). Macro-, meso-, and micro-structures can be constructed using the above-mentioned processes. Specifically, (i) soft materials are obtained by the process of printing thermosensitive and photosensitive hydrogels; (ii) hard materials are obtained by the processes of fused deposition modeling, solution electrospinning (SE), and near-field melt electrospinning; and (iii) multiscale fiber filaments include coarse fiber filaments, fine fiber filaments, and nanofiber filaments. Thick fiber filaments are obtained by fused deposition modeling process, thin fiber filaments are obtained by near-field melt electrospinning process, and nanofiber filaments are obtained by SE process; (iv) macro- and meso-scale structures are obtained by direct printing of thermo- and photo-sensitive hydrogels, fused deposition modeling; (v) the micro-scale structures are obtained by near-field melt electrospinning; and (vi) the micro-scale structures are obtained by the process of SE. Material delivery in all of the above processes is achieved by microextrusion, and we use three enabling technologies (motor-driven piston-based microextrusion, pneumatic-based microextrusion, and mechanical screw-based) to meet the demand for more materials.

2.2. Implementation methods for multifunctional modular 3D bioprinting system

The 3D bioprinting system supported by an intelligent PAD usually includes an intelligent PAD-driven printer main control board (which is used to output the printing parameters of the designed model, including materials, printing speed, and motion parameters), a built-in customized application to control the system, and could communicate through Bluetooth. To make it more accessible to the general use, implementing cost-effective hardware will be decisive (since smart PADs are now common and available everywhere, they are not included in the cost analysis). It is worth mentioning that the maximum printing size is 90 × 90 × 50 mm, although the overall size of the device is relatively small (300 × 300 × 300 mm, **Figure 3A**), it does not make the size of the printable samples very small. In the field of 3D bioprinting, this size is sufficient. Microextrusion-based nozzles use mechanical (piston or screw) or pneumatic dispensing systems to extrude continuous bioink (materials and/or cells). The mechanical piston **Figure 3H** and screw are driven by the motor, and the pneumatic extrusion is driven by the external compressed air. As shown in **Figure 3A**, the 3D bioprinting platform can mount 3 types of nozzles at the same time.

2.2.1. Integrated motion system

The 3D motion module designed in this study is relatively compact, and the motions in the three directions of XYZ are driven by stepper motors (**Figure 3B,F)**. For each printing layer, the Z direction advances the distance of one layer. This turns 3D printing into two-dimensional (2D) printing within each plane. 2D printing within each plane is also driven by stepper motors. As shown in **Figure 3A**, movement in the X direction is achieved by the rotation of stepping motor A and driving the linear displacement stage, and movement in the Y direction is achieved by the rotation of stepping motor B and driving the linear displacement stage. The three nozzles are fixed on the slider of the linear guide moving in the X direction, the linear guide moving in the X direction is fixed on the slider of the linear guide moving in the Y direction, and the modeling platform (**Figure 3A**, the white tablet is marked with a "G") is fixed on the printer base with no freedom of movement. Each

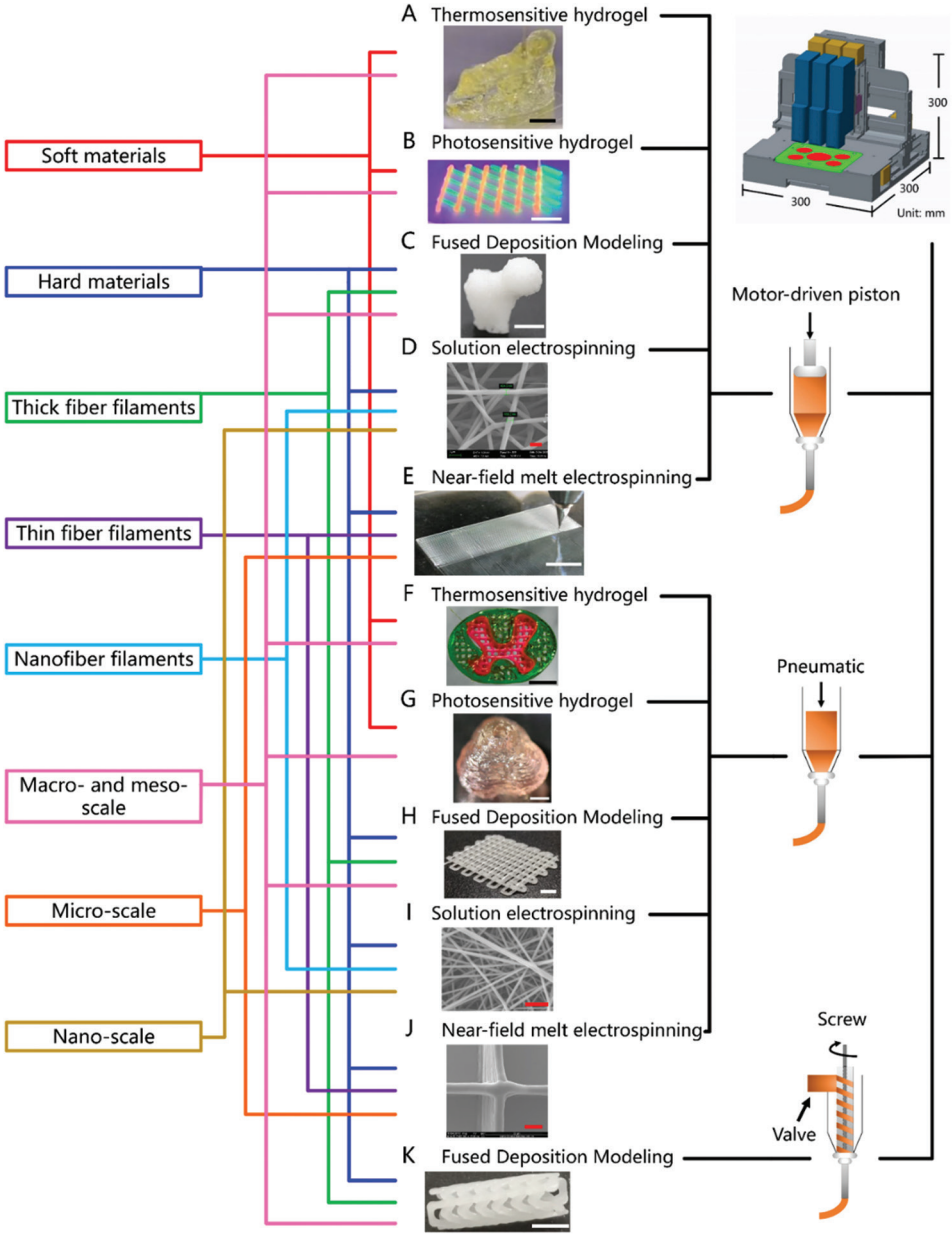

Figure 2. Schematic of the microextrusion-based multifunctional modular 3D bioprinting system. The system can print soft materials, hard materials, and multiscale fiber filaments. Three enabling technologies, including motor-driven pistons, pneumatic-driven pistons, and mechanical screw extrusion, were used for printing strategies. Scale bar: 5 mm (A, B, C, E, F, G, H, K), 1 μm (D), 2 μm (I), and 10 μm (J).

nozzle is mounted on the slider of the linear guide moving in the Z direction. All nozzles of the printer in this paper have three degrees of freedom of movement. The above design ensures the function while minimizing the overall volume.

2.2.2. Modular design and fabrication of materials delivery system

(A) Motor-driven piston-based microextrusion nozzles

In the motor-driven piston-based microextrusion process, the piston in the syringe loaded with bioink material was pushed through the linear movement of the motor, which, then, produced volume changes and ejected forward. The design schematic diagram of motor-driven piston-based microextrusion processes is shown in **Figure 4A-F**. The motor extrusion type can precisely control the distance of the motor movement to control the precise change in the syringe volume and, then, produce a precise volume of material injection. The advantage of using a single integrated circuit board to control dozens of motors makes the size of the entire

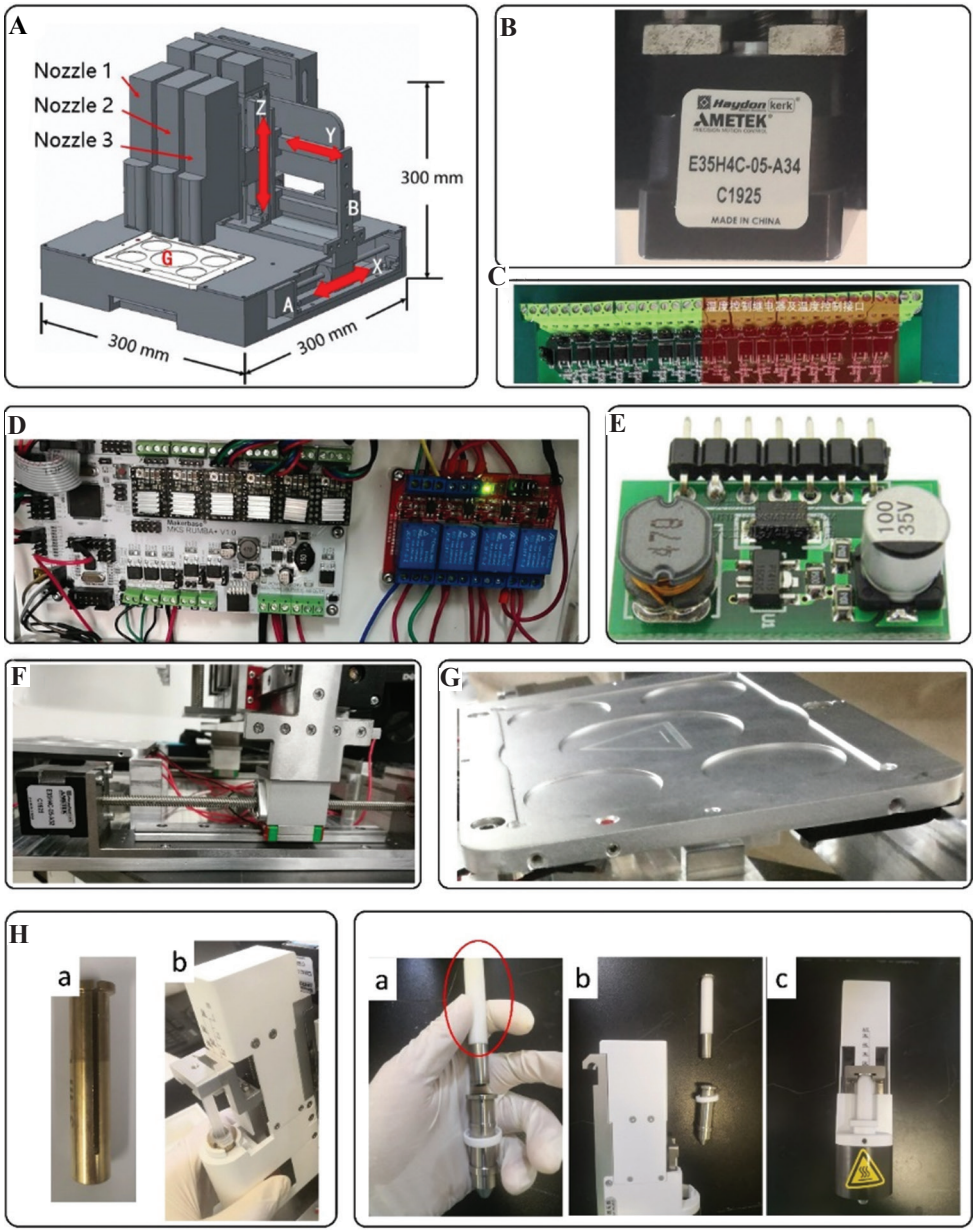

Figure 3. Several key supporting technologies enable the proper functioning of the 3D bioprinting system. (A) Schematic of the 3D bioprinting system. Stepper motor (B), temperature control relay and temperature control interface (C), system hardware mainboard (D), LED light source PWM controller (E), X-direction movement displacement slide (F), print bed (G), motor-driven nozzle (H, thermal sleeves suitable for various types of syringes [a]), and motor-driven fused deposition modeling nozzle (I, stainless steel syringe [a], insulated plunger [red marked]).

electronic control system very small, which provides a foundation for the miniaturization and modularization of the nozzles. The UV curing module was embedded in the material ejection outlet position of the nozzles, which facilitated timely and accurate light cross-linking of the photosensitive hydrogel. The size of the entire nozzle is 30 mm × 85 mm × 170 mm in width, length, and height, respectively. The width of 30 mm made it possible to mount three nozzles on the motion platform at the same time.

(B) Pneumatic-based microextrusion nozzles

Pneumatic extrusion material injection injects materials through air pressure with appropriate pressure. The process is simple to control and only requires the opening and closing of the air valve. We chose a gas cylinder commonly used in laboratories as the source of compressed gas, resulting in a small size and almost no noise. The design schematic diagram of pneumatic-based microextrusion processes is shown in **Figure 4G-K**.

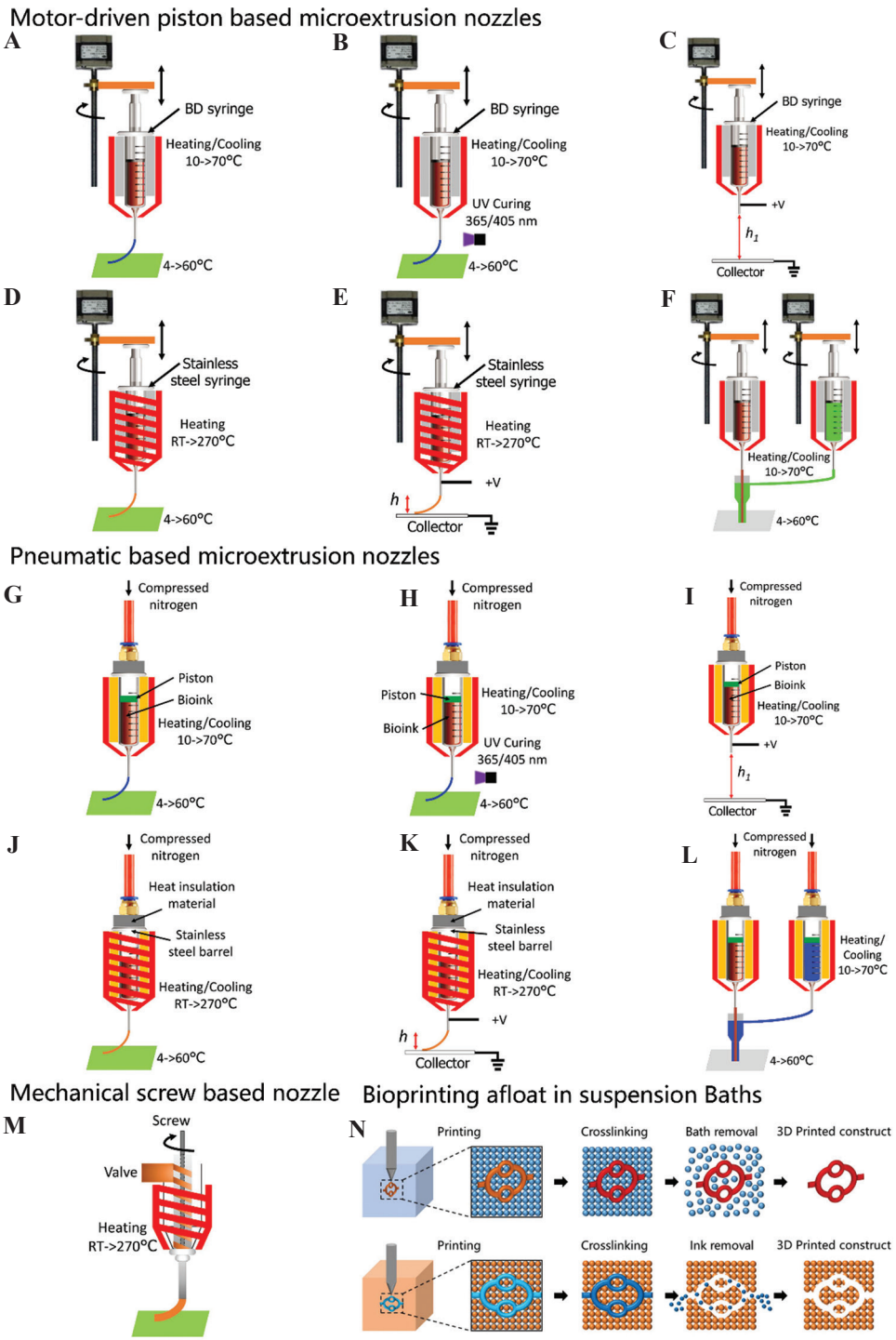

Figure 4. Schematic of the modular designed nozzles. (A-F) Motor-driven piston-based microextrusion nozzles. (G-L) Pneumatic microextrusion nozzles. Nozzles for printing thermosensitive (A and G) and photosensitive (B and H) hydrogels, nozzles for fused deposition modeling (D and J), nozzles for solution electrospinning (C and I) and near-field electrohydrodynamic direct writing (E and K), and nozzles for coaxial printing (F and L). (M) Mechanical screw-based nozzle. (N) Overview of the 3D printing pathways of printing in a suspension medium. Pathway is defined by removal of the medium after printing (top) and retention of the medium after printing (bottom).

Through the adjustment of the multistage pressure reducing valve, a pressure of 0.005 – 1 MPa can be provided. The bioink materials can be extruded by directly supplying air pressure to the pneumatic piston syringe (**Figure 4G-I and L**). When printing cell-containing bioinks, a rubber piston must be installed as a buffer to prevent high

pressure from damaging the cells. In the FDM process, polymer pellets were loaded into a stainless steel syringe and then melted, and the compressed gas acted directly on the molten material (**Figure 4J and K**). This design does not need to consider the resistance of the piston to high temperatures, and the bubbles in the material will be eliminated. Compared with the mechanical piston driven by a motor, the printing method has significant advantages in eliminating bubbles.

(C) Mechanical screw-based nozzle

During the screw extrusion process, the material chamber will not change in volume, and the material can be continuously fed for a long time, which is suitable for printing biological materials with high viscosity and easy precipitation. The temperature of the material in the screw can be controlled by wrapping a heating resistor on the periphery of the screw (**Figure 4M**).

(D) Concentricity maintaining structure designed for coaxial printing

The key to the success of the inner and outer nesting structure of the coaxial extrusion cell printing nozzle is to ensure that the relative positions of the inner and outer needles are not eccentric. Therefore, a triangular claw structure was designed to ensure its coaxiality. Due to different bioink materials, the success of printing in the coaxial nozzle also depends on the height difference between the inner and outer needles. The height difference between the inner and outer needles was designed in an adjustable way to facilitate printing with different materials. Another problem often encountered in actual use of coaxial printing is the problem of nozzle clogging. The difference between this research and other research designs is that we designed the coaxiality guaranteed structure on the outer sprinkler. The inner diameter of the outer nozzle is designed to be larger and easy to clean and can be used non-disposably. The inner diameter of the inner nozzle is very thin and not easy to clean, so we use a disposable standard syringe steel needle, which can reduce the difficulty of cleaning the nozzle and reduce the cost of use. In the subsequent printing test experiments, the inner diameter of the final needle used was 0.33 mm, and the inner diameter of the outer needle was 1.1 mm.

2.2.3. Multifunctional additive manufacturing platform

The additive manufacturing platform designed in this research realizes two-way temperature control with both cooling and heating functions and adopts the temperature control system of the forming platform, in which the heating sheet and the semiconductor cooling sheet are compounded. The heat dissipation system of the additive manufacturing platform is set directly below it, which will not pollute the printed samples. The additive manufacturing platform of 3D printing is usually a flat plate, but cell printing is a special printing environment that needs to prevent bacterial contamination, and its commonly used carrier vessels include Petri dishes and well plates. Among them, the diameters of commonly used Petri dishes are 35 mm, 60 mm, and 90 mm, and the diameters of commonly used orifice plates are 6-well plates, 12-well plates, 24-well plates, 96-well plates, and so on. To allow users to accurately use the abovementioned various types of Petri dishes and well plates when using the printer, this research developed a multifunctional additive manufacturing platform that uses the groove structure to locate different Petri dishes and well plates (secured with elastic claw structure) (**Figure 3G**).

2.2.4. Accurate positioning and temperature control device

Using an infrared laser sensor and mechanical position sensor composite software system, the system allows the nozzle (the outlet position of the extruded material on the nozzle) tip position of all nozzles to be corrected in 3D space. We designed and manufactured rapid temperature change controls. Semiconductor refrigeration and resistance heating are used to provide temperature control for the nozzles and the print bed **Figure 5**. Each nozzle was equipped with a temperature control device. There are two specifications, one of which has a temperature control range of 10 – 70°C (with heating and cooling functions, which can quickly adjust the temperature, ~10°C/min) used for low-viscosity materials, and the other has a temperature control range of RT-270°C (heating up fast (>20°C/min) cooling down slowly (~6°C/min)) was designed for the FDM process. For the (10 – 70°C) temperature control devices, the heating unit used a ceramic heater, and the cooling unit used semiconductor refrigeration with an air-cooled device. For the (RT-270°C) temperature control devices, the heating unit used a resistance wire with a spiral sleeve shape, and a powerful air-cooled heat dissipation system was designed to dissipate heat in the non-heated area, which could reduce the impact of the high-temperature environment on the nozzle motor and other electronic components. The print bed equipped with a temperature control device (range of 10 – 60°C), which has heating (used a ceramic heater) and cooling (used semiconductor refrigeration) functions, makes the heating and cooling process very fast. The temperature control error is 0.1°C ([10 – 70 °C] and [10 – 60°C]) and 1°C ([RT-270°C]).

2.2.5. Integrated hardware control system

During the research and development process, we chose the Arduino Mega 2560 chip as the mother board, which has strong development and expansion

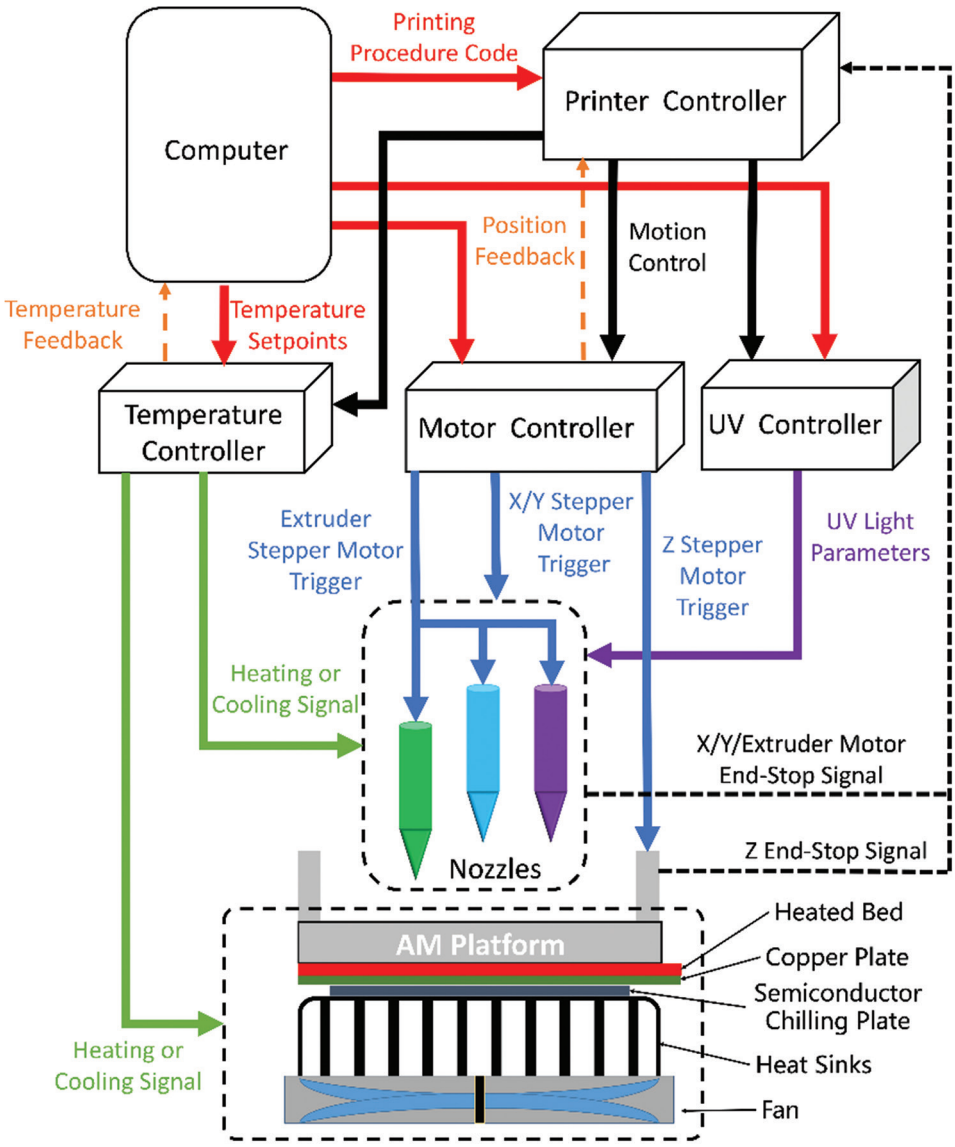

Figure 5. The links between the various units and the direction of flow of the control signals are shown schematically for the multifunctional modular 3D bioprinting system.

capabilities. The stepper motor controller used in the printer developed in this paper is TMC2209, with a maximum of 256 subdivisions and a maximum current of 2.5 A. Compared with common stepping motor controllers, the selected controller is smaller in size, approximately 1/10 the size of common stepping motor drivers (**Figure 3D**), greatly reducing the space of the equipment. Conventional temperature control functions are mostly realized by temperature control meters, but the large size of temperature control meters is not suitable for the development of miniaturized 3D printing equipment. The integrated control system we developed integrates the functions of the thermostat into the control board and is connected to the interface of the temperature sensor, the heating plate, and the cooling plate (**Figure 3C**). The temperature setting and temperature display functions are realized by the host computer software, which greatly reduces the volume of the entire temperature control device. Common biological 3D printers use industrial UV light source control systems with high power. We chose a 3 W LED light source (providing a range of light intensities: 0 – 50 mW/cm^2 and approximately 1/100 of the volume of industrial light sources) as the UV light source for material light curing. Using the integrated control board developed by us, the variable control of light source power can be realized (**Figure 3E**), and the overall volume of the device can be greatly reduced.

2.2.6. Customized software enables the application of the desired print control

This software system is divided into two control modes, (i) standard mode: first select the 3D model (external source or built-in model), then perform layering, then explore process parameters, and finally print the structure and (ii) Quick mode: prestore the optimized data model containing printing process information in the common database so that users can skip redundant steps and quickly start the repeated printing of the model when they use it for the 2nd time. The printer software interface enables the input of required printing parameters and the automatic generation of g-codes to appropriately move and trigger the motion system and nozzles. The temperature and UV control interface allow one to set the nozzle's temperature, UV curing intensity, and duration.

2.2.7. Integrated technology for modular and collaborative printing

Nozzles that can be quickly replaced are an important foundation for modular combinations of nozzles. The print head often contains functions such as temperature control and extrusion control, so the connection between the print head and the main body of the printer has not only a mechanical connection but also an electronic interface. The common mechanical connection method is screw connection. The connection is firm, but it is inconvenient to disassemble. Therefore, this study intends to explore a way to quickly replace and combine multifunctional nozzles. A quick-release joint (a fixed method of magnetic attraction and POGO PIN electronic interface) was used to connect the motion system and achieve the signal transmission. When using the magnetic attraction method of plane bonding, if the magnetic attraction is too small, the nozzle will easily shake naturally, resulting in poor stability. If the magnetic attraction is too large, it is not easy to assemble the nozzles. Therefore, in this study, a "ㄱ"-shaped suspension mode was designed. The "convex" shape designed on the top of the back plate matches the "concave" shape structure on the back of the nozzle, which not only provides nozzle upward force support but also limits the possibility of swinging from side to side. Using the combination design of magnets and the matching design of the POGO PIN, the nozzle can be quickly connected and removed from the motion system (within 3 s).

3. Initial experiments and prefabrication printing results of a single nozzle

To further explore the capability of this multifunctional modular 3D bioprinting system, the printability, fidelity, and resolution were subsequently evaluated. To achieve soft and hard materials, multiscale fiber filaments, and multiscale structures, the printing effects of the developed system in terms of temperature-sensitive biological ink, photosensitive biological ink, high-temperature stent printing, high-temperature stent and hydrogel composite printing, coaxial printing, and suspension printing will be verified. The related printing parameters of the extrusion cell printing process, such as nozzle diameter, printing speed, ejection speed, printing path spacing, and height, affect the formability of the cell printing ink and the cell survival rate, as shown in a previous article[59,60]. Therefore, this research will not perform further exploration in this area. Initial experiments and prefabricated printing results are described below.

3.1. Printing thermosensitive hydrogels

To print a 3D complex cell structure with high-resolution, the cell printing ink needs to improve the gel capacity of the bioink by increasing the viscoelasticity of the printing ink to maintain the mechanical properties of the stacked structure. However, as the viscoelasticity of the cell printing ink increases, the shear force that the cells are subjected to during the printing process increases, thereby reducing the survival rate of the cells. Therefore, controlling the viscoelasticity of the cell printing ink during the printing process and finding the appropriate viscoelastic interval of the cell printing ink are important steps to achieve good cell 3D printing (good formability and biological performance). Temperature can control the temperature-sensitive material in the gel or sol state and then affects the viscoelasticity of the material.

The rheological properties of gelatin, silica gel, GelMA, and PF127 were tested before printing to determine the optimal printing temperature of the materials (**Figure 6A-D**). Various structures were printed using 10% (w/t)gelatin at 22°C and as shown in **Figure 6E**. About 40% (w/t) PF127 (Pluronic F-127, Dow Corning) was printed at 18°C to verify the printer's ability to print complex structures (**Figure 6F**). Gelatin, silica gel, nanocellulose, and PF127 material were used to print (motor-driven piston-based microextrusion) the complex shape of the human ear structure, as shown in **Figure 7A**. The pneumatic-based microextrusion nozzle was also tested using PF127, GelMA to print mesh (**Figure 7B[i]**), cervical stent (**Figure 7B[ii]**), and spinal cord (**Figure 7B[iii]**) structures. The above results show that the printed model maintains a high fidelity. A mixed bioink containing 10% (w/t) gelatin, 1% (w/t) sodium alginate, and cells (1 × 10^6 cells/mL) mL)(the rheologicalparameters as shown in **Figure 6G** was used to print the mesh structures (**Figure 6H**), and the survival rate of printed cells (A549, HeLa, NIH3T3 and HUVECs) was tested afterward. After printing, the cell survival rate exceeded 80% (**Figure 6I-M**), meeting the requirements for further use. Actin staining results of HeLa cells as shown in **Figure 6N**.

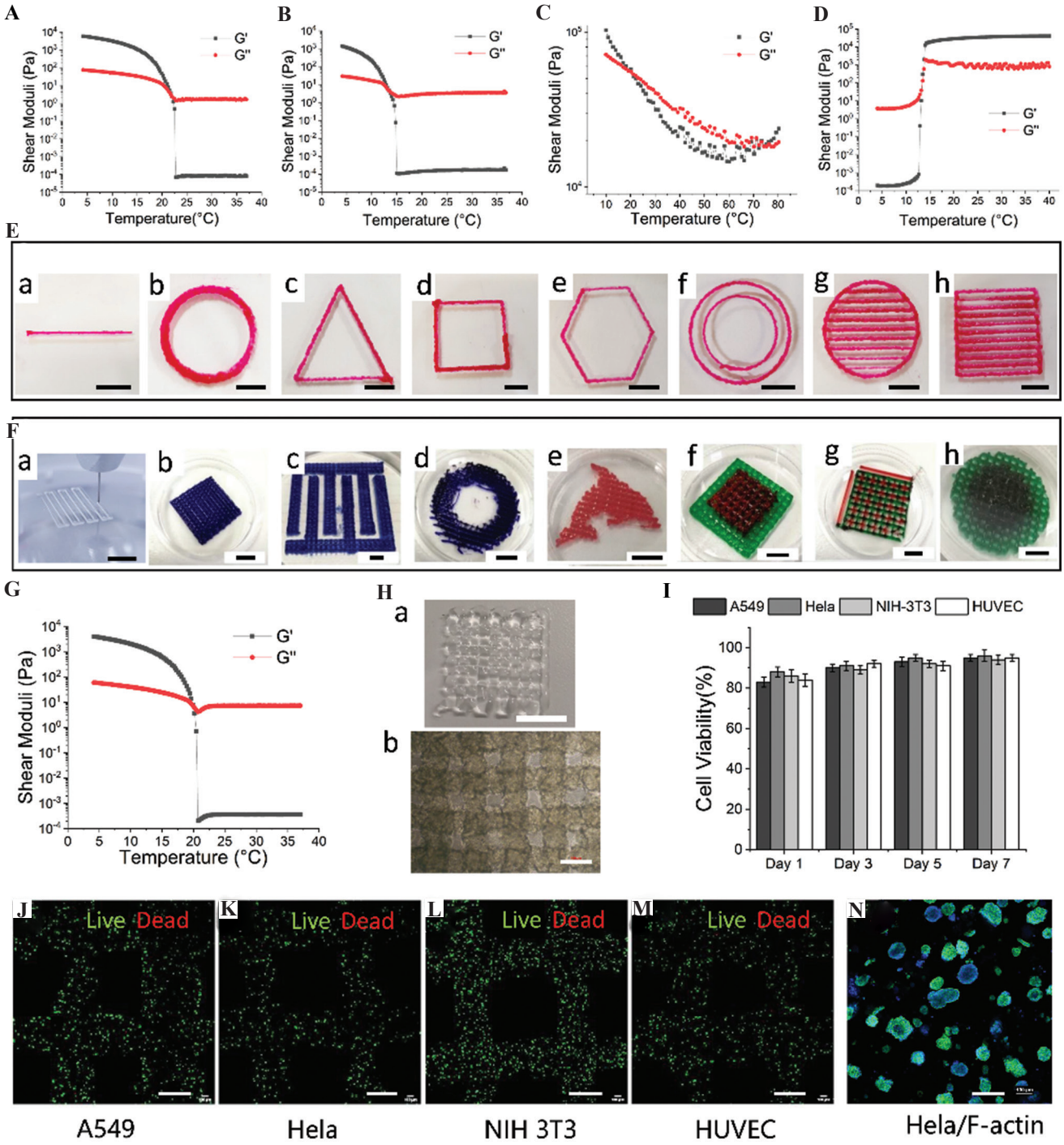

Figure 6. Initial experiments of printing thermosensitive hydrogels. The rheological properties of gelatin (A), GelMA (B), silica gel (C), and PF127 (D). (E) A series of structures were printed using gelatin ink to verify the printability of the system. (F) PF127 (40% [w/t]) (Pluronic F-127, Dow Corning) was printed at 18°C to verify the printer's ability to print complex structures. Structures of grids (a, b, c), rings (d), dolphins (e), dual-material stacked grids (f), alternately printed grids with dual nozzles (g), and three stacked grids printed with three nozzles (h). (G) Rheological properties of gelatin (10% [w/t]) sodium alginate (1% [w/t]) bioinks. (H) Grid structures printed using gelatin (10% [w/t]) sodium alginate (1% [w/t]). (I) Survival rate of printed cells (A549 [J], HeLa [K], NIH3T3 [L] and HUVECs [M]). (N) Actin staining results of HeLa cells (day 7). Scale bar: 5 mm (E, F, H [a]), 100 μm (H [b]), 500 μm (J, K, L, M), and 200 μm (N).

3.2. Printing photosensitive hydrogel

GelMA is a commonly used photosensitive biomaterial, which is gelatin methacrylated. In this section, GelMA will be used as a photosensitive hydrogel bioink to verify the printing ability of the cell 3D printing system developed in this paper in terms of photosensitive ink.

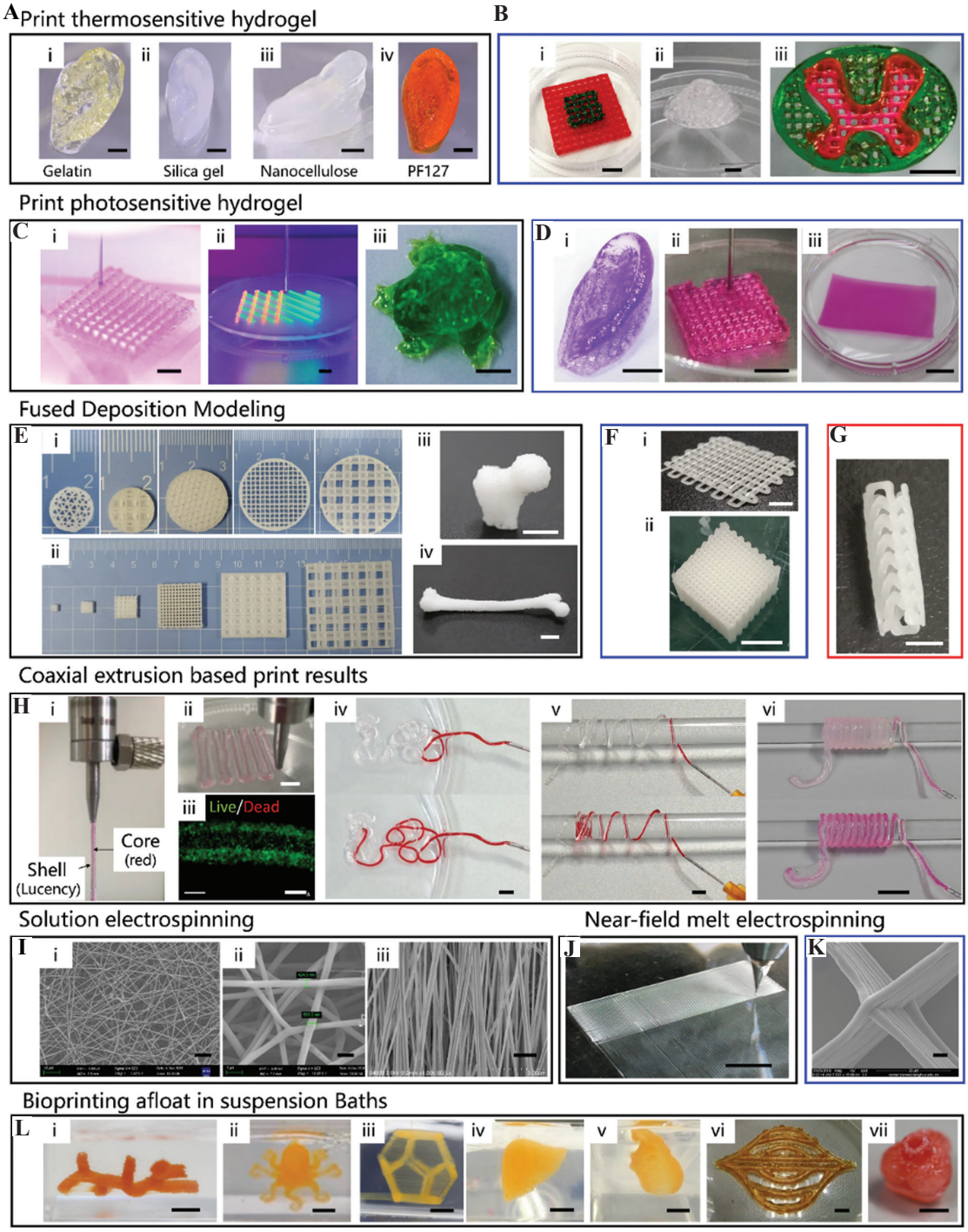

Figure 7. Initial experiments and prefabricated printing results. Three enabling technologies of motor-driven pistons (within the black rectangle), pneumatic-driven pistons (within the blue rectangle), and mechanical screw extrusion (within the red rectangle) were used. (A) Gelatin, silica gel, nanocellulose, and PF127 material were used to print human ear structures. (B) Results of printed mesh ([i], PF127), cervical stent ([ii], GelMA), and spinal cord ([iii], GelMA) structures. (C) Structure printed with GelMA material. Single-nozzle printed grid scaffolds (i). Double nozzles alternately print grid structures (ii). Complex 3D structures (turtle model) printed with a single nozzle (iii). (D) Printing results of pneumatic microextrusion, models of ear (i), mesh (ii), and multilayer hydrogel skin-like structure (iii). (E-G) Fused deposition modeling of PCL structures. (H) Coaxial extrusion results of a perfusable tubular structure. Solution electrospinning (I) and near-field melt electrospinning (J and K). (L) Suspension media used as technological aid for 3D bioprinting of vascular branch structure (i), octopus model (ii), hollow polyhedral structure outline (iii), liver contour stent (iv), heart contour stent (v), unilateral structure model of vascular axis section (vi), and salivary gland (vii). Scale bar: 5 mm (A, B, C, D, E, F, G, H [ii, iv, v, vi], J, L), 500 μm (H[iii]), 10 μm (I[i], K), 1 μm (I[ii]), and 2 μm (I[iii]).

The previous work has introduced the effect of UV light irradiation on the biological activity of the cells in printed structures when GelMA is used as a bioink[61,62]. Therefore, this section uses the previous experimental conclusions to directly verify the structure printing capability of the system and the cell survival rate after printing.

According to the results of rheological analysis (**Figure 8B, C**), the gel point of GelMA used in the experiment can be obtained at 23°C. GelMA ink (10% [w/t]) was used for printing tests based on motor-driven microextrusion (mesh and turtle models, **Figure 7C**) and pneumatic microextrusion (models of ear, mesh, and multilayer hydrogel skin-like structure, **Figure 7D**). GelMA (10% [w/t]) was also used to print the structural models of elephant head and spinal cord (**Figure 8A**). It can be seen from these results that the printing structure is well formed and has high stability and fidelity. The configured GelMA$^+$ bioink (with cells) was loaded on the nozzle of the printing system and the predesigned computer 3D structure was printed under the condition that the temperature of the

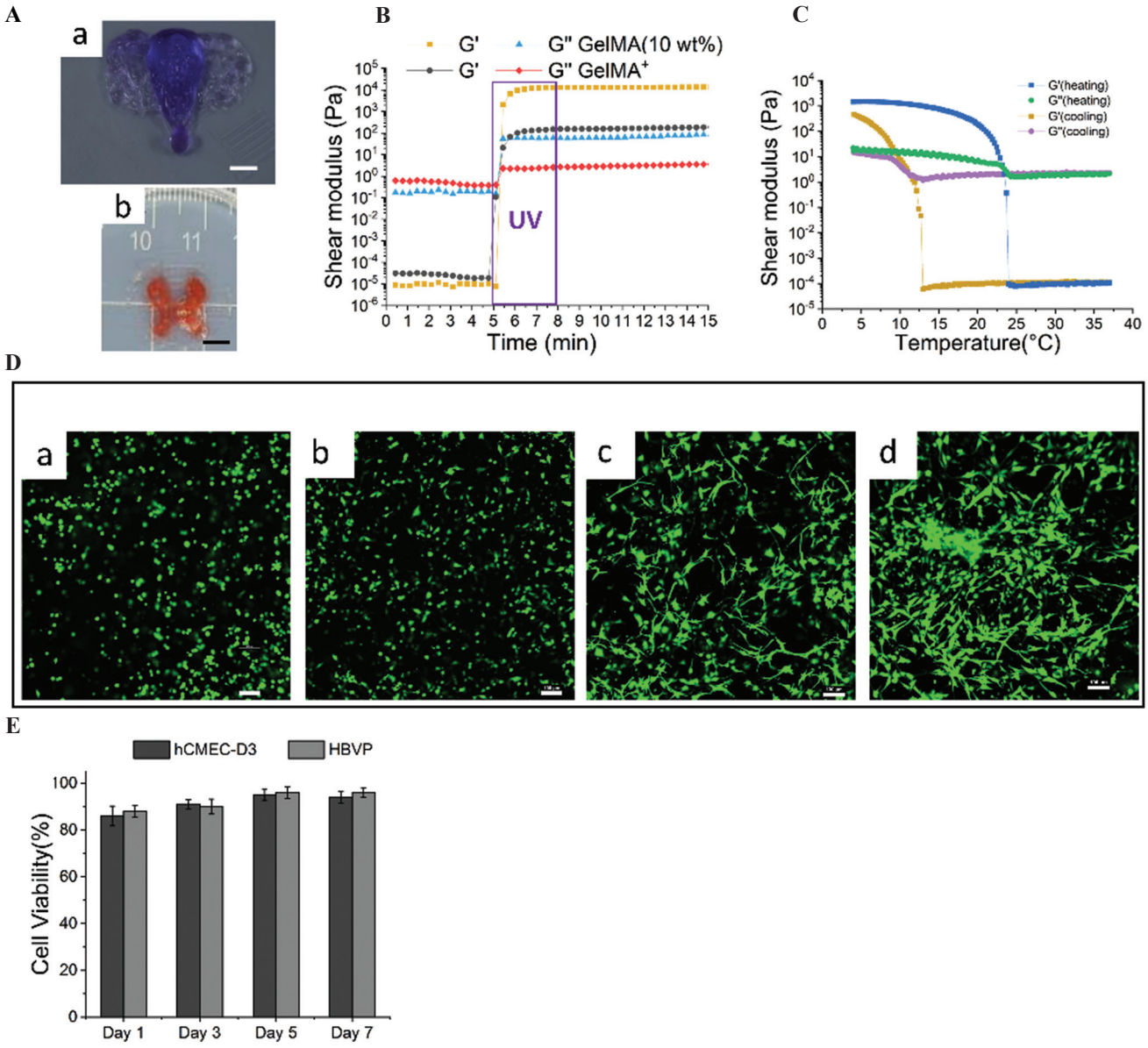

Figure 8. Initial experiments of printing photosensitive hydrogels. (A) GelMA (10% [w/t]) was also used to print the structure models of elephant head (a) and spinal cord (b). (B) The result of photo cross-linking resulting in altered rheological properties of GelMA (10% [w/t]) and GelMA$^+$ (composed of 2.5% [w/t] GelMA, 5% [w/t] gelatin, 5 mg/mL fibrinogen, and 0.25% (w/t) LAP/mL). (C) Rheology results of GelMA (10% [w/t]). (D) GelMA+ ink containing HBVP-GFP (GFP-labeled cells) was used to print grid structures and for up to 7 days of culture observation. Cell morphology of HBVP-GFP on day 1 (a), day 3 (b), day 5 (c), and day 7 (d). (E) Cell viability of hCMEC/D3 and HBVP-GFP cells during 7 days of culture. Scale bar: 5 mm (A), 500 μm (D).

print head is 24°C (the needle size is 25 G, the movement speed of the nozzle is 5 mm/s, and the ejection speed is 0.8 mm^3/s). After printing, the 365 nm blue light that comes with the nozzle head was used to irradiate it at 5 mW/cm^2 for 30 s. The printed sample was incubated in an incubator for more than 20 min to stabilize the structure, and then, a picture was taken with a digital camera with a macro lens for observation or further incubation. $GelMA^+$ ink containing HBVP-GFP (GFP-labeled cells) was used to print grid structures and for up to 7 days of culture observation. On days 1, 3, 5, and 7, the cell morphology (**Figure 8D**) and cell viability (**Figure 8E**) were detected. The cell survival rate of hCMEC/D3 and HBVP cells after printing exceeded 80%, which met the requirements for further use. The cells in the hydrogel began to stretch on the 3rd day, and some cells joined together on the 7th day (**Figure 8D[a-d]**). This shows that the printing process does not cause damage to the cells. Therefore, the photo cross-linking material-based printing nozzle developed in this paper meets the basic printing needs.

3.3. Fused deposition modeling

PCL has the characteristics of a low melting point (~60°C), degradability, and good biocompatibility. It has also been approved by the FDA and is an ideal material for biological 3D printing stents. Because the melting point of PCL is relatively low, the temperature will soon drop below 37°C, which is not damaging to the cells, after hot melt printing.

In this system, three printing methods based on motor driven pistons, pneumatic driven pistons, and mechanical screw extrusion are developed for fused deposition modeling. The printing results of these three nozzles were tested. The results of different inner diameter nozzles on the diameter of the printed PCL are shown in **Figure 9** (using a motor-driven piston-based microextrusion nozzle). For the nozzle with an inner diameter of 200 μm, the measured printing filament diameter is 197.11 ± 37.93 μm (**Figure 9A**). For the nozzle with an inner diameter of 300 μm, the measured printing filament diameter is 295.67 ± 37.94 μm (**Figure 9B**). For the nozzle with an inner diameter of 400 μm, the measured printing filament diameter is 432.00 ± 72.64 μm (**Figure 9C**). For the nozzle with an inner diameter of 600 μm, the measured printing filament diameter is 499.34 ± 110.85 μm (**Figure 9D**). For the nozzle with an inner diameter of 800 μm, the measured printing filament diameter is 624.18 ± 114.35 μm (**Figure 9E**). On the basis of these process data, the ability to print complex PCL structures is further verified. Including square and circular structures with different filling styles and sizes, brackets for the femoral head, and tibial model structures were printed using a motor-driven piston-based microextrusion nozzle (**Figure 7E**). Two-layer grid supports and cube-shaped scaffolds were printed using a pneumatic extrusion nozzle (**Figure 7F**, the gas pressure was 0.5 ~ 0.6 MPa). Cardiovascular stents were printed using a mechanical screw-based nozzle (**Figure 7G**). The above results showed that this printing system has good forming quality in the formation of complex PCL structures.

3.4. Coaxial printing results

Coaxial extrusion bioprinting is an emerging branch of bioprinting that shows strong potential in enhancing the engineering versatility of bioprinting. Coaxial bioprinting facilitates the fabrication of complex tissue structures by enabling the concentric deposition of biomaterials. It was initially applied to fabricate simple tubular vasculature but has now largely evolved to integrate complex cellular composition and self-assembly, ECM patterning structures, controlled release, and multimaterial gradient profiles[63].

Before printing, the configured bioink was loaded on the two nozzles (30% [w/t] PF127 in inner, 10% [w/t]

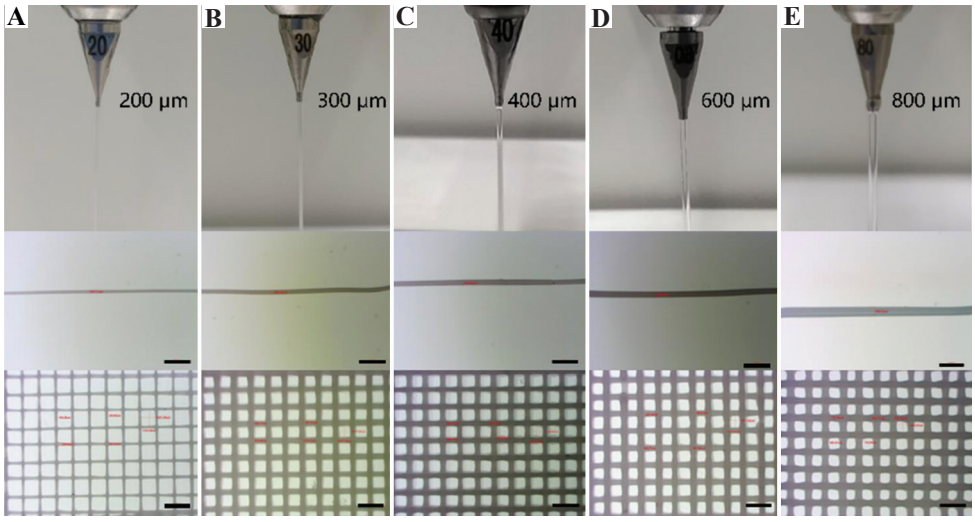

Figure 9. The results of different inner diameter nozzles on the diameter of the printed PCL. Scale bar: 2 mm.

GelMA, and 1% [w/t] alginate in outer) of the coaxial nozzle of the printing system. When the temperature of the nozzle reached 20°C, the predesigned computer 3D structure was printed (the nozzle movement speed was 5 mm/s, the ejection speed was 0.4 mm^3/s for the inner nozzle, and 3.6 mm^3/s for the outer nozzle). Then, 365 nm blue light was used with the nozzle to irradiate at 5 mW/cm^2 for 30 s of curing or 3% $CaCl_2$ soaking for 3 min to cure. **Figure 7H** shows the printing capability of the cell 3D printing system developed in this paper in coaxial printing applications. From the results, it can be seen that the shape is coherent, the internal and external structures are clear, and the mechanical strength supports perfusion. The connectivity of the printed tubular structure shows that the tubular structure printed with the coaxial nozzle has good connectivity. At the same time, using 10% (w/t) GelMA and 1% alginic acid bioink to print BMSC cells, a good tubular structure was formed, and the survival rate of printed cells was more than 90%.

3.5. Electrohydrodynamic spinning

Due to the flexible design of the mounting position of the printing nozzle, the maximum distance between the nozzle and the printing platform can reach more than 10 cm. Therefore, the system can be applied to medium field electrospinning (distance approximately 1 ~ 10 cm) and near-field melt electrospinning (distance approximately i 1 cm). During SE, the PCL solution is loaded into a syringe driven by a motor-driven piston, and the solution is then extruded from the needle tip of the 21G syringe at a constant rate. Taylor cones can be formed after applying a high-voltage electric field (5 – 15 kV) between the needle and the collector, which, in turn, generates disordered nanofiber filaments on the platform (**Figure 7I[i]**). Nanofiber filaments are approximately 500 nm in diameter (**Figure 7I[ii]**). When the nozzle is installed obliquely on the motion system and a double thin disk collector is placed at a relatively long distance (>10 cm), the application of an electric field can generate oriented nanofiber filaments (**Figure 7I[iii]**).

It is ground-breaking to increase the controllability of a single fiber by reducing the needle-to-collector distance from more than 10 cm to less than 1 cm. It is possible to control and operate a single electrospinning fiber, including the position, shape, and morphology of a single electrospinning fiber[64]. Near-field electrospinning printing is suitable for melt printing but not for solution printing. Therefore, we first used a motor-driven metal push rod to extrude the material for testing and conducted a printing experimental study on the near-field electrospinning process, in which the high-pressure gas directly drives the material extrusion. During near-field melt electrospinning, the supplied gas pressure is approximately 10 kPa. The experimental results show that both motor-driven (**Figure 7J**) and pneumatic extrusion (**Figure 7K**) materials can print micron-scale diameter filaments with good orientation. The diameter of the filaments is approximately 5 μm (**Figure 7K**). During the printing process, the distance between the needle and the collector was approximately 3.5 mm, and the applied voltage was approximately 3 kV. The moving speed of the nozzle is 40 mm/s. It is worth mentioning that air humidity and temperature affect the electric field strength required to generate stable filaments, as well as the distance between the needle and the collector.

3.6. Bioprinting afloat in suspension baths

Suspension printing (floating printing) is a 3D printing method that has recently emerged and does not require a traditional support structure[65]. Instead of depositing material on a flat surface in the air, it places the printed material in a suspension tank that prevents the material from settling and collapsing (**Figure 4N**). We verified the feasibility of the multifunctional modular 3D bioprinting system developed in this paper in suspension printing. Steps of printing structure in the suspension glue are as follows: first, load the configured GelMA bioink on the print head of the printing system. When the temperature of the nozzle is 20°C, the syringe is installed with a 1-inch length needle (25G) and penetrates into the suspension glue. Second, print out the predesigned computer 3D structure (the movement speed of the nozzle is 5 mm/s, and the ejection speed is 0.8 mm^3/s). Finally, 365 nm blue light that comes with the nozzle was used to irradiate the printed 3D structure for 30 s at 5 mW/cm^2. After the 3D structure sample was printed, it was removed with tweezers and then immediately washed with water or sodium chloride.

In the suspension printing process, a series of complex structures are printed, such as vascular branch structures (**Figure 7L[i]**), octopus models (**Figure 7L[ii]**), hollow polyhedral structure outlines (**Figure 7L[iii]**), liver contour stents (**Figure 7L[iv]**), heart contour stents (**Figure 7L[v]**), unilateral structures of vascular axis sections (**Figure 7L[vi]**), and salivary glands (**Figure 7L[vii]**). The above results fully demonstrate the ability of the cell 3D printing system developed in this paper to print complex structures in suspension glue. It can be seen from the results that the forming is good, and various complex structures and even nested structures can be formed to meet the requirements of use. Furthermore, HepG2 cells (bioink, 10% [w/t] GelMA) were printed in suspension glue to build grid stents, and the cell survival rate was tested. The results showed that the cell survival rate after printing exceeded 80%, which met the requirements for further use.

4. Coupling results of using multiprinting technology

Next, in the developed multifunctional modular bioprinting system, four synergistic printing processes were explored,

including (i) multi-material printing combining hard and soft materials through fused deposition printing and hydrogel printing; (ii) multiscale structure printing combining thick fiber and nanofiber filaments through fused deposition printing and electrospinning processes; (iii) the combination of temperature cross-linking, covalent bond crosslinking and ionic bond crosslinking; and (iv) the fabrication of hierarchical structures based on suspension printing.

4.1. Multi-material printing of combining hard and soft materials

PCL and GelMA composite printing were used to verify the feasibility of the multifunctional cell 3D printing system developed in this paper in the composite printing of scaffolds and cells. PCL particles (Sigma, 45,000 molecular weight) were loaded into the high-temperature printing nozzle, and the structure was printed under the condition of a nozzle holding temperature of 10°C (the nozzle movement speed was 5 mm/s, and the ejection speed was 0.5 mm^3/s). Then, the configured GelMA biological ink was loaded on the print head of the printing system, and the structure was printed under the condition that the temperature of the print head was 20°C (the movement speed of the print head was 5 mm/s, and the ejection speed was 0.8 mm^3/s). A schematic diagram of the detailed printing operation steps is shown in **Figure 10A**. After printing, a 365 nm UV lamp was used with the nozzle to irradiate it for 30 s at 5 mW/cm^2. The results of the composite structure of PCL and GelMA hydrogel are shown in **Figure 10B**. Including the ring (**Figure 10C**), meniscus (**Figure 10D**), and caput femoris structure (**Figure 10E**), the printing system has good printing ability in the composite printing of stents and hydrogels. This process includes the printing of hydrogel materials at low temperature and the printing of polymer material PCL at high temperature. The local and small-scale switching of the two printing environments will expand the printing applications in more scenarios in the future. It needs to be discussed that the material printed by fused deposition modeling in this experiment is PCL with a low melting point. After PCL is extruded from the nozzle, it cools down quickly so that the cells in the hydrogel are less damaged. If it is a material with a high melting point, it will possibly result in higher cell death rate after printing.

4.2. Multiscale structure printing of combining thick fiber and nanofiber filaments

Combining fused deposition modeling and electrospinning printing, polymer filament structures with two fiber diameter scales can be fabricated. The filaments with a diameter of micrometers provide mechanical support for the entire scaffold structure, and the filaments with a diameter of nanometers provide adhesion points and microenvironments for cells. In this experiment, the material for melt extrusion printing was PCL, and the material for electrospinning was PCL/collagen solution. PCL/collagen solution was prepared by dissolving 10 g PCL and 7.5 g collagen in 100 mL HFIP. In the printing process test, we printed nanofiber filaments on melt extrusion-printed PCL scaffolds to form a nanofiber blanket. A schematic diagram of the printing process is shown in **Figure 10F**. HUVECs-T1 was seeded on a nanofiber blanket, and further, culture observations were performed for up to 7 days. The scanning electron microscope results showed that the cells were well attached to the nanofiber blanket (**Figure 10G[i-v]**). Immunofluorescence staining of nuclei and F-actin showed that the cells were well connected and grew into one piece (**Figure 10G[vi]**).

4.3. Multi-material printing of integrating various cross-linking methods

Next, we implemented the process of multiple cross-linking modalities in the same printing experiment. In the experiment, two printing nozzles based on motor-driven piston extrusion were used, one of which was printed with $Gelatin^+$ (7.5% [w/t] gelatin and 100 U/mL thrombin) and the other with $GelMA^+$ (composed of 2.5% [w/t] GelMA, 5% [w/t] gelatin, 5 mg/mL fibrinogen, and 0.25% [w/t] LAP/mL). Since fibrinogen and thrombin will quickly cross-link to form a gel within tens of seconds, they cannot be mixed in a silo. After the materials were prepared, hCMEC/D3 cells were mixed into $GelMA^+$ ink, mixed, and then loaded into a disposable BD syringe. A 25 G half-inch stainless steel sterilized needle was installed, and then, the syringe was loaded into the nozzle. The nozzle temperature was set to 22°C, and the platform temperature was set to 18°C. A schematic diagram of the printing process is shown in **Figure 10H** (various cross-linking methods during the printing process as shown in **Figure 10I**). After the grid structure was printed, UV cross-linking was performed for 30 s. Then, the grid structure sample was incubated in a carbon dioxide incubator for 20 min, which was helpful for the complete binding of fibrinogen and thrombin. The printed samples were then incubated and observed for up to 16 days. hCMEC/D3 cells were labeled with GFP to facilitate long-term culture observation of cell morphology without damage. The results showed that hCMEC/D3 cells grew well in $GelMA^+$ bioink, some cells stretched on day 4, cells were fully stretched, and some cells were connected together on day 7, and the results on day 16 showed that cells formed networks and

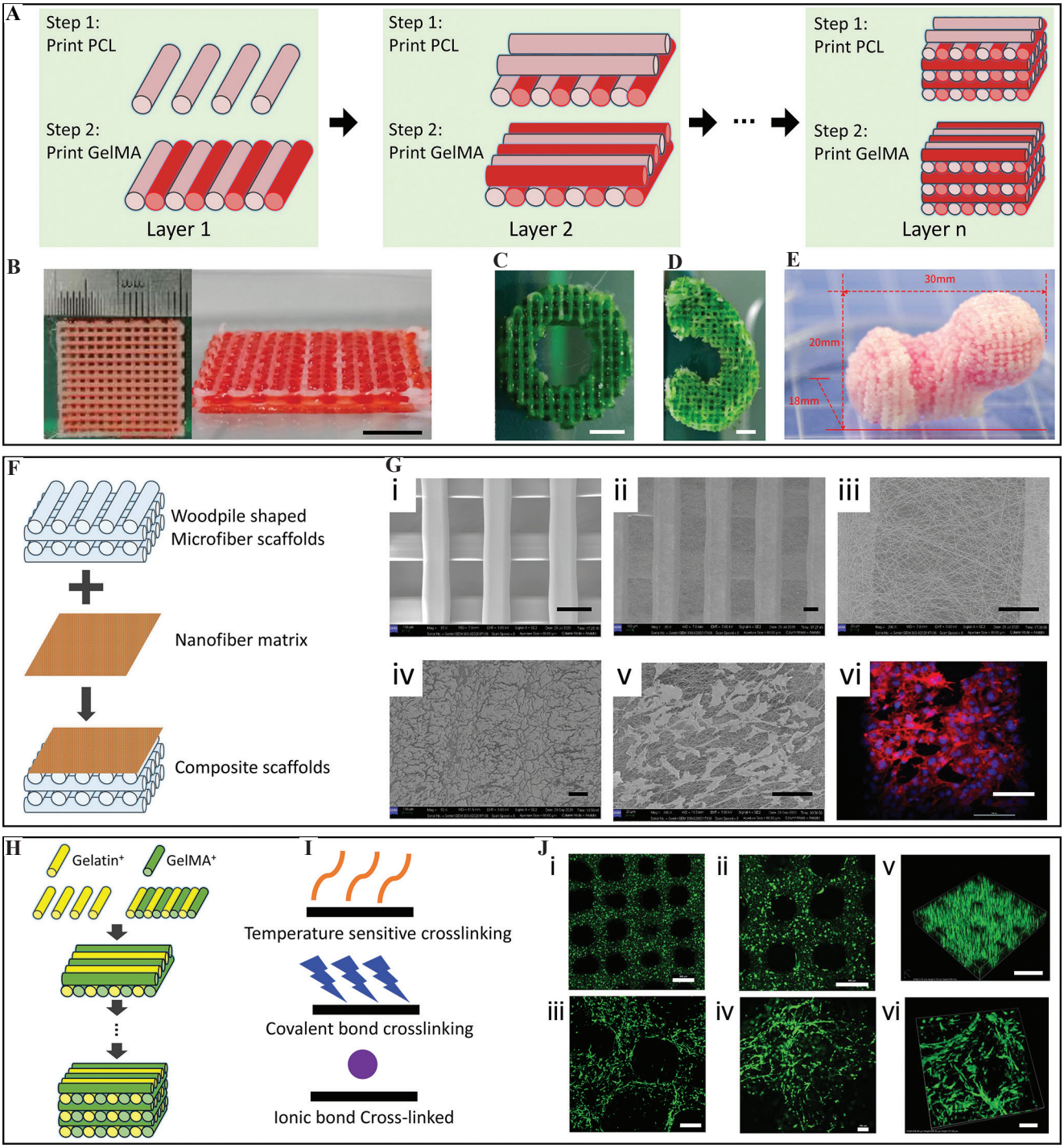

Figure 10. Coupling results of using multiple nozzles. (A) Manufacturing process of composite scaffold hybrid printing of PCL and GelMA. Image of PCL and GelMA hybrid structures, mesh (B), ring (C), meniscus (D), caput femoris (E), schematic (F), and image results (G) of the combination of high-temperature fused deposition printing and electrospinning processes. (H, I) Schematic of the combination of various cross-linking methods during the printing process. (J) Cell morphology results in printed grids, day 1 (i), day 4 (ii), day 7 (iii), and day 16 (iv). Scale bar: 5 mm (B-D,), 500 µm (G[i], J[i, ii]), 200 µm (G[ii, iv], J[iii]), 100 µm (G[iii, v, vi], J[iv, vi]), and 1 mm (J[v]).

began to degenerate (**Figure 10J**). Confocal 3D scans show that cells are well stretched and grow together in the hydrogel, enabling cell-to-cell connections (**Figure. 10J[i-vi]**).

5. Conclusion

We have developed an unprecedented multifunctional modular 3D bioprinting system, a smart tablet based on

Bluetooth communication and a customized printing operation program, enabling us to realize a variety of 3D bioprinting processes (based on motor-driven piston extrusion, pneumatic driven piston extrusion, and mechanical screw extrusion based on three power drive modes) in a small space (300 mm × 300 mm ×300 mm) with a high level of automation and accuracy. The software and hardware are modularized. Standardized and modular designs are made for the nozzle, molding environment, drive system, bioink cartridge (silo), light curing module, etc. The printing nozzles were fixed on the developed 3D motion platform as required and could be used alternately in a print program. To achieve soft and hard materials, multiscale fiber filaments, and multiscale structures, the system realizes the printing of thermosensitive and photosensitive hydrogels, the fused deposition modeling of polymers, SE, near-field electrohydrodynamic direct-writing, and other process integrated operations on only one platform. The experimental results demonstrate that the printed material can cover commercially available hard polymers and soft hydrogels, satisfying a wide range of applications. This system increases the scope and research potential of these material and fabrication technology combinations. Initial experiments and prefabricated sample construction validate the system's strong potential application in custom scaffold fabrication due to its modular design and ability to integrate any available printing mode in a single fabrication session. We highlight that this printing platform has significant advantages, including portability, modularity, and an easy-to-use interface. We reasonably envision the great potential of our multifunctional modular full-scene application printer in various fields, such as medicine, biomedicine, education, and space experiments.

Data availability statement

All data that support the findings of this study are included within the article.

Funding

National Key Research and Development Program of China (2018YFA0703004).

Conflicts of interest

No conflicts of interest were reported by all authors.

Authors' contributions

Conceptualization: Wei Sun,Ting Zhang,Yuanyuan Xu
Investigation: Yuanyuan Xu,Chengjin Wang,Hui Liu
Methodology: Yuanyuan Xu
Formal analysis: Yuanyuan Xu
Writing – original draft: Yuanyuan Xu
Writing – review & editing: Wei Sun,Zhuo Xiong,Ting Zhang,Yang Yang

References

1. Donald E. Ingber, 2016, Reverse Engineering Human Pathophysiology with Organs-on-Chips. *Cell*, 164:1105–9. https://doi.org/10.1016/j.cell.2016.02.049
2. Atala A, 2020, Introduction: 3D printing for biomaterials. *Chem Rev*, 120:10545–6. https://doi.org/10.1021/acs.chemrev.0c00139
3. Ouyang L, Yao R, Zhao Y, *et al.*, 2016, Effect of bioink properties on printability and cell viability for 3D bioplotting of embryonic stem cells. *Biofabrication*, 8:035020. https://doi.org/10.1088/1758-5090/8/3/035020
4. Ouyang L, Yao R, Mao S, *et al*., 2015, Three-dimensional bioprinting of embryonic stem cells directs high-throughput and highly uniform embryoid body formation. *Biofabrication*, 7:044101. http://doi.org/10.1088/1758-5090/7/4/04410
5. Sun W, Starly B, Daly AC, *et al.*, 2020, The bioprinting roadmap. *Biofabrication*, 12:022002 https://doi.org/10.1088/1758-5090/ab5158
6. Murphy SV, Atala A, 2014, 3D bioprinting of tissues and organs. *Nat Biotechnol*, 32:773–85. https://doi.org/10.1038/nbt.2958
7. Kang HW, Lee SJ, Ko IK, *et al*., 2016, A 3D bioprinting system to produce human-scale tissue constructs with structural integrity. *Nat Biotechnol*. 34:312–9. https://doi.org/10.1038/nbt.3413
8. Jorgensen AM, Yoo JJ, Atala A, 2020, Solid organ bioprinting: Strategies to achieve organ function. *Chem Rev*, 120:11093–127. https://doi.org/10.1021/acs.chemrev.0c00145
9. Mikos AG, Herring SW, Ochareon P, *et al*., 2006, Engineering complex tissues. *Tissue Eng*, 12:3307–39. https://doi.org/10.1089/ten.2006.12.3307
10. Atala A, Kasper FK, Mikos AG, 2012, Engineering complex tissues. *Sci Transl Med*, 4:160rv12. https://doi.org/10.1126/scitranslmed.3004890
11. Nemir S, West JL, 2010, Synthetic materials in the study of cell response to substrate rigidity. *Ann Biomed Eng*, 38:2–20. https://doi.org/10.1007/s10439-009-9811-1
12. Kim HN, Kang DH, Kim MS, *et al*., 2012, Patterning methods for polymers in cell and tissue engineering. *Ann Biomed Eng*, 40:1339–55.
13. Karimi A, Shojaei A, 2017, Measurement of the mechanical properties of the human kidney. *IRBM*, 38:292–7. https://doi.org/10.1016/j.irbm.2017.08.001
14. Umale S, Deck C, Bourdet N, *et al.*, 2013, Experimental mechanical characterization of abdominal organs: Liver,

kidney & spleen. *J Mech Beha Biomed Mater*, 17:22–33. https://doi.org/10.1016/j.jmbbm.2012.07.010

15. Thubrikar M, Piepgrass WC, Bosher LP, *et al*., 1980, The elastic modulus of canine aortic valve leaflets *in vivo* and *in vitro*. *Circ Res*, 47:792–800. https://doi.org/10.1161/01.res.47.5.792
16. Thubrikar MJ, Aouad J, Nolan SP, 1986, Comparison of the *in vivo* and *in vitro* mechanical properties of aortic valve leaflets. *J Thorac Cardiovasc Surg*, 92:29–36.
17. Silver FH, Kato YP, Ohno M, *et al*., 1992, Analysis of mammalian connective tissue: relationship between hierarchical structures and mechanical properties. *J Long Term Eff Med Implants*, 2:165–98.
18. Cua AB, Wilhelm KP, Maibach HI, 1990, Elastic properties of human skin: Relation to age, sex, and anatomical region. *Arch Dermatol Res*, 282:283–8. https://doi.org/10.1007/BF00375720
19. Abe H, Hayashi K, Sato M, 1996, Data Book on Mechanical Properties of Living Cells, Tissues, and Organs. Tokyo: Springer.
20. Akhtar R, Sherratt MJ, Cruickshank JK, *et al*., 2011, Characterizing the elastic properties of tissues. *Mater Today (Kidlington)*, 14:96–105. https://doi.org/10.1016/S1369-7021(11)70059-1
21. Arda K, Ciledag N, Aribas BK, *et al*., 2013, Quantitative assessment of the elasticity values of liver with shear wave ultrasonographic elastography. *Indian J Med Res*, 137:911–5.
22. Yeh WC, Li PC, Jeng YM, *et al*., 2002, Elastic modulus measurements of human liver and correlation with pathology. *Ultrasound Med Biol*, 28:467–74. https://doi.org/10.1016/s0301-5629(02)00489-1
23. Krouskop TA, Wheeler TM, Kallel F, *et al*., 1998, Elastic moduli of breast and prostate tissues under compression. *Ultrason Imaging*, 20:260–74. https://doi.org/10.1177/016173469802000403
24. Mikula ER, Jester JV, Juhasz T, 2016, Measurement of an elasticity map in the human cornea. *Invest Ophthalmol Vis Sci*, 57:3282–6.
25. Qin X, Tian L, Zhang H, *et al.*, 2019, Evaluation of corneal elastic modulus based on Corneal Visualization Scheimpflug Technology. *Biomed Eng Online*, 18:42. https://doi.org/10.1186/s12938-019-0662-1
26. Samani A, Zubovits J, Plewes D, 2007, Elastic moduli of normal and pathological human breast tissues: An inversion-technique-based investigation of 169 samples. *Phys Med Biol*, 52:1565–76. https://doi.org/10.1088/0031-9155/52/6/002
27. Gefena A, Dilmoney B, 2007, Mechanics of the normal woman's breast. *Technol Health Care*, 15:259–71.
28. Martin RB, Burr DB, Sharkey NA, 1998, Mechanical properties of ligament and tendon. In: Skeletal Tissue Mechanics. New York, NY: Springer.
29. Maganaris CN, Paul JP, 1999, *In vivo* human tendon mechanical properties. *J Physiol*, 521:307-13. https://doi.org/10.1111/j.1469-7793.1999.00307.x
30. Wu D, Isaksson P, Ferguson SJ, *et al*., 2018, Young's modulus of trabecular bone at the tissue level: A review. *Acta Biomater*, 78:1–12. https://doi.org/10.1016/j.actbio.2018.08.001
31. Gefen A, Margulies SS, 2004, Are *in vivo* and *in situ* brain tissues mechanically similar? *J Biomech*. 37:1339–52. https://doi.org/10.1016/j.jbiomech.2003.12.032
32. Budday S, Nay R, de Rooij R, *et al*., 2015, Mechanical properties of gray and white matter brain tissue by indentation. *J Mech Behav Biomed Mater*, 46:318–30. https://doi.org/10.1016/j.jmbbm.2015.02.024
33. Morin F, Chabanas M, Courtecuisse H, *et al*., 2017, Biomechanical modeling of brain soft tissues for medical applications. *Biomech Living Organs*, 2017:127–46.
34. Boschetti F, Pennati G, Gervaso F, *et al*., 2004, Biomechanical properties of human articular cartilage under compressive loads. *Biorheology*, 41:159–66.
35. Xu YY, Guo X, Yang ST, *et al*., 2018, Construction of bionic tissue engineering cartilage scaffold based on three-dimensional printing and oriented frozen technology. *J Biomed Mater Res A*, 106:1664–76. https://doi.org/10.1002/jbm.a.36368
36. Lefèvre E, Baron C, Pithioux M, 2013, Evaluation of the elastic modulus of cortical bone: adaptation of experimental protocols to small samples. *Comput Methods Biomech Biomed Engin*, 16 Suppl 1:328–9. https://doi.org/10.1080/10255842.2013.815945
37. Rudolph AS, 1994, Biomaterial biotechnology using self-assembled lipid microstructures. *J Cell Biochem*, 56:183–7. https://doi.org/10.1002/jcb.240560211
38. Stupp SI, 2010, Self-assembly and biomaterials. *Nano Lett*, 10:4783–6. https://doi.org/10.1021/nl103567y
39. Raub CB, Putnam AJ, Tromberg BJ, *et al*., 2010, Predicting bulk mechanical properties of cellularized collagen gels using multiphoton microscopy. *Acta Biomater*, 6:4657–65. https://doi.org/10.1016/j.actbio.2010.07.004
40. McBane JE, Vulesevic B, Padavan DT, *et al*., 2013, Evaluation of a collagen-chitosan hydrogel for potential use as a pro-angiogenic site for islet transplantation. *PLoS One*, 8:e77538. https://doi.org/10.1371/journal.pone.0077538
41. Murphy KC, Leach JK, 2012, A reproducible, high throughput

method for fabricating fibrin gels. *BMC Res Notes*, 5:423. https://doi.org/10.1186/1756-0500-5-423

42. EzEldeen M, Toprakhisar B, Murgia D, *et al*., 2021, Chlorite oxidized oxyamylose differentially influences the microstructure of fibrin and self-assembling peptide hydrogels as well as dental pulp stem cell behavior. *Sci Rep*, 11:5687. https://doi.org/10.1038/s41598-021-84405-4
43. Kong HJ, Smith MK, Mooney DJ, 2003, Designing alginate hydrogels to maintain viability of immobilized cells. *Biomaterials*, 24:4023–9. https://doi.org/10.1016/s0142-9612(03)00295-3
44. Patois E, Cruz SO, Tille J, *et al*., 2009, Novel thermosensitive chitosan hydrogels: *In vivo* evaluation. *J Biomed Mater Res A*, 91:324–30. https://doi.org/10.1002/jbm.a.32211
45. Soares LS, Gomes BT, Miliao GL, *et al*., 2021, Mixed starch/chitosan hydrogels: Elastic properties as modelled through simulated annealing algorithm and their ability to strongly reduce yellow sunset (INS 110) release. *Carbohydr Polym*, 255:117526. https://doi.org/10.1016/j.carbpol.2020.117526
46. Park S, Goodman BM, Pruitt BL, 2005, Measurement of Mechanical Properties of Caenorhabditis elegans with a Piezoresistive Microcantilever System. 3rd IEEE/EMBS Special Topic Conference on Microtechnology in Medicine and Biology, p. 400–3.
47. Li Z, Reimer C, Wang T, *et al*., 2020, Thermal and Mechanical Properties of the Biocomposites of Miscanthus Biocarbon and Poly(3-Hydroxybutyrate-co-3-Hydroxyvalerate) (PHBV). *Polymers*, 12:1300. https://doi.org/10.3390/polym12061300
48. Carvalho C, Landers R, Muelhaupt R, 2004, Soft and hard implant fabrication using 3D-bioplotting. *SFF Symp Proc.*, 732–741.
49. Ligon SC, Liska R, Stampfl J, *et al*., 2017, Polymers for 3D printing and customized additive manufacturing. *Chem Rev*, 117:10212–90. https://doi.org/10.1021/acs.chemrev.7b00074
50. Zhu Y, Joralmon D, Shan W, *et al.*, 2021, 3D printing biomimetic materials and structures for biomedical applications. *Biodes Manuf*, 4:405–28.
51. Rawal P, Tripathi DM, Ramakrishna S, *et al.*, 2021, Prospects for 3D bioprinting of organoids. *Biodes Manuf*, 4:627–40.
52. Zhang YS, Ghazaleh H, Tania H, *et al*., 2021, 3D extrusion bioprinting. *Nat Rev Methods Primers*, 1:75.
53. Zhang YS, Khademhosseini A, 2020, Engineering *in vitro* human tissue models through bio-design and manufacturing. *Biodes Manuf*, 3:155–9.
54. He Y, Nie J, Xie M, *et al.*, 2020, Why choose 3D bioprinting? Part III: Printing *in vitro* 3D models for drug screening. *Biodes Manuf*, 3:160–3.
55. Zhou J, Tian Z, Tian QY, *et al*., 2021, 3D bioprinting of a biomimetic meniscal scaffold for application in tissue engineering. *Bioact Mater*, 6:1711–26. https://doi.org/10.1016/j.bioactmat.2020.11.027
56. Kolesky DB, Truby RL, Gladman AS, *et al*., 2014, 3D bioprinting of vascularized, heterogeneous cell-laden tissue constructs. *Adv Mater*, 26:3124–30. https://doi.org/10.1002/adma.201305506
57. Ouyang L, Armstrong JP, Chen Q, *et al*., 2020, Void-free 3D bioprinting for *in-situ* endothelialization and microfluidic perfusion. *Adv Funct Mater*, 30:1908349. https://doi.org/10.1002/adfm.201908349
58. Wang C, Xu Y, Xia J, *et al*., 2021, Multi-scale hierarchical scaffolds with aligned micro-fibers for promoting cell alignment. *Biomed Mater*. 16:045047. https://doi.org/10.1088/1748-605X/ac0a90
59. Li SJ, 2009, Studies on Three Dimensional Controlled Multi-Cell Assembling Technology. Beijing: Tsinghua University.
60. Khalil S, Nam J, Sun W, 2005, Multi, a university dimensional controlled multi-cell assembling technology. *B Rapid Prototyp J*, 11:9–17.
61. Zhao Y, 2017, Fundamental Research and Application Based on Integration of 3D Cell Printing and Microfluidic and Chip Manufacturing. Beijing, Tsinghua University.
62. Ouyang L, 2017, Studies on Microextrusive 3D Bioprinting Based on Bioink Crosslinking Mechanism. Beijing, Tsinghua University.
63. Kjar A, McFarland B, Mecham K, *et al*., 2021, Engineering of tissue constructs using coaxial bioprinting. *Bioact Mater*, 6:460–71.
64. Huang YA, Bu NB, Duan YQ, *et al*., 2013, Electrohydrodynamic direct-writing. *Nanoscale*, 5;12007.
65. McCormack A, Highley CB, Leslie NR, *et al*., 2020, 3D printing in suspension baths: Keeping the promises of bioprinting afloat. *Trends Biotechnol*, 38:584–93. https://doi.org/10.1016/j.tibtech.2019.12.020

Publisher's note